The Effect of Cohesive-Law Parameters on Mixed-Mode Fracture

R. B. Sills[*§] and M. D. Thouless[*†]

[*]*Department of Mechanical Engineering*
[†]*Department of Materials Science & Engineering*
University of Michigan
Ann Arbor, MI 48109-2125, USA

Abstract

Cohesive-zone models of fracture provide a framework that allows a smooth transition between a strength-based approach to fracture and an energy-based approach. At the heart of these models are traction-separation laws that are described by a cohesive strength and toughness. These cohesive-law parameters can be used to define a cohesive-length scale that, when compared to physical length scales in the problem, gives an indication of whether failure is controlled by strength or energy considerations. Mixed-mode fracture is described by a phase angle that provides a measure of the partition of the deformation energy into shear and normal components. It is shown that this phase angle can be calculated for a cohesive-zone model, and that, if the cohesive length is small enough, the phase angle agrees with the value predicted by linear-elastic fracture mechanics, irrespective of the shape of the cohesive-laws. It is further shown that the cohesive length derived from the cohesive parameters can be used to rationalize the concept of a phase angle for interfacial fracture in the presence of a modulus mismatch. In particular, the length scale required to define a phase angle for interfacial fracture can be identified with the cohesive length of a cohesive-zone model. This phase angle shifts with changes in the cohesive length in accordance to the predictions of linear-elastic interfacial fracture mechanics.

(October 4, 2011)
(Revised: May 30, 2012)

Keywords: mixed-mode; phase angle; cohesive-zone; fracture; modulus mismatch; cohesive length

[§] Current address: *Gas Transfer Systems, Sandia National Laboratories, Livermore, CA 94550 USA*

1. Introduction

Cohesive-zone models of fracture provide a framework that allows a smooth transition between the strength-based approach of Inglis [1913] to fracture, and the energy-based approach of Griffith [1920]. At the heart of these models are the cohesive stresses that provide bonding across an interface or putative crack plane. These stresses are described by a traction-separation law that is characterized by a cohesive strength (peak stress) and toughness (area under the traction-separation curve). Under pure mode-I loading, the cohesive strength, $\hat{\sigma}$, toughness, Γ_I, and elastic modulus of the material adjacent to the crack plane, $\overline{E}$, can be combined to define a nominal cohesive length [Hillerborg *et al.*, 1976; Bao and Suo, 1992]:

$$\zeta_I = \overline{E}\Gamma_I / \hat{\sigma}^2 \quad , \tag{1}$$

where $\overline{E} = E/\left(1-\nu^2\right)$ in plane strain, $\overline{E} = E$ in plane stress, and E and ν are Young's modulus and Poisson's ratio, respectively. This nominal cohesive length provides an indication of whether failure is controlled by strength or energy considerations. When ζ_I is much smaller than the characteristic geometrical lengths, crack propagation is controlled only by the energy considerations. Under these conditions, linear-elastic fracture mechanics (LEFM) provides a well-understood basis for describing fracture, and toughness is the important failure parameter. Conversely, when ζ_I is much greater than the characteristic geometrical lengths, crack propagation is controlled only by stress considerations, and the cohesive strength controls failure. Under intermediate conditions, both the strength and toughness influence the conditions for crack growth.

Within the LEFM framework for analyzing crack propagation, the cohesive strength is assumed to be infinite, and there is no concept of a cohesive length. This

means that there is no length scale associated with the fracture process. As explained below, this can result in a well-known conundrum for a crack growing along an interface between two dissimilar materials, since there are conditions under which LEFM cannot be used to analyze crack growth without invoking the existence of a cohesive length.

The modulus mismatch across a planar, isotropic, bimaterial interface (Fig. 1) can be described by the two Dundurs parameters [Dundurs, 1969],

$$\alpha = \frac{\bar{E}_1 - \bar{E}_2}{\bar{E}_1 + \bar{E}_2} \tag{2a}$$

and

$$\beta = \frac{\bar{E}_1 f(\nu_2) - \bar{E}_2 f(\nu_1)}{\bar{E}_1 + \bar{E}_2} \quad , \tag{2b}$$

where the subscripts 1 and 2 denote the materials on either side of the interface, $f(\nu) = (1-2\nu)/[2(1-\nu)]$ in plane strain, and $f(\nu) = (1-2\nu)/2$ in plane stress. The expression for the normal stress, σ_{yy}, and shear stress, σ_{xy}, on the interface at a distance r immediately ahead of a crack tip is given by [Rice, 1988]

$$(\sigma_{yy} + i\sigma_{xy}) = Kr^{i\varepsilon}/\sqrt{2\pi r} \tag{3a}$$

where,

$$\varepsilon = \frac{1}{2\pi}\ln\left(\frac{1-\beta}{1+\beta}\right) \tag{3b}$$

and K is a complex stress-intensity factor with real, Re(K), and imaginary, Im(K), parts, related by a phase angle ψ_K. The phase angle is a function of a characteristic dimension, L, of the geometry, and is of the form

$$\psi_K = \tan^{-1}[\mathrm{Im}(K)/\mathrm{Re}(K)] = \omega - \varepsilon \ln L \ , \tag{4}$$

where ω depends on the geometry and loading. When β and, hence, ε = 0, this expression is well defined. However, the phase angle becomes dependent on the choice of units for length if β ≠ 0!

The energy-release rate, $\mathcal{G}$, which is the energetic driving force for crack propagation, is related to the stress-intensity factor by

$$\mathcal{G} = \frac{\left(1-\beta^2\right)}{\overline{E}^*}\left|K\right|^2 = \frac{1}{\overline{E}^* \cosh^2 \pi\varepsilon}\left|K\right|^2 \quad , \tag{5}$$

where $|K|$ is the magnitude of K, and $\overline{E}^*$ is the characteristic modulus of a bi-material system:

$$\overline{E}^* = \frac{2\overline{E}_1\overline{E}_2}{\overline{E}_1+\overline{E}_2} = \left(1-\alpha\right)\overline{E}_1. \tag{6}$$

Following the Griffith assumption of fracture [Griffith, 1920], crack propagation along the interface occurs when the energy-release rate exceeds a critical value known as the interfacial toughness, Γ. The concept of a phase angle enters the analysis of crack propagation because there is extensive experimental evidence that the interfacial toughness is not a fixed material parameter, but depends on the loading and geometry through the phase angle [Cao and Evans, 1989; Wang and Suo, 1990; Thouless, 1990; Thouless, 1992; Liechti and Chai, 1992]. This concept, known as a "mode-dependent toughness" or a "mixed-mode failure criterion," is used in LEFM analyses and predictions of interfacial crack propagation.

If the Dundurs parameter β is zero, the real and imaginary parts of the stress-intensity factor are uniquely identified as the mode-I and mode-II components, K_I and K_{II}, of the stress-intensity factor, with each component independently describing the normal and shear deformations along the interface. These normal and shear deformations can

also be associated with the mode-I and mode-II components of the energy-release rate, $\mathcal{G}_I = K_I^2 / \overline{E}^*$ and $\mathcal{G}_{II} = K_{II}^2 / \overline{E}^*$, respectively, so that the phase angle can be written as[1]

$$\psi_K = \psi^\infty = \tan^{-1}\left(K_{II} / K_I\right) = \tan^{-1}\left(\sqrt{\mathcal{G}_{II} / \mathcal{G}_I}\right) = \omega \quad . \tag{7}$$

The problem associated with the definition of a phase angle in LEFM solutions for bi-material interfaces when $\beta \neq 0$ has long been recognized [Comninou, 1990]. It arises because there is no length scale in the mathematical formulation of linear-elastic fracture mechanics that can be used to normalize the characteristic dimension in Eqn. 4. One approach to resolve this difficulty is the introduction of an arbitrary length, ξ, into the formulation of the problem. The phase angle of the product $K\xi^{i\varepsilon}$ is then well-defined [Rice, 1988], and can be used as the nominal phase angle:

$$\psi^\infty = \tan^{-1}\left[\frac{\mathrm{Im}\left(K\xi^{i\varepsilon}\right)}{\mathrm{Re}\left(K\xi^{i\varepsilon}\right)}\right] \quad . \tag{8}$$

This nominal phase angle is related to the phase angle ψ_K of Eqn. 4 by

$$\psi^\infty = \psi_K + \varepsilon \ln\left(\xi / L\right) \quad . \tag{9}$$

However, any attempt to link ψ^∞ to a mixed-mode failure criterion depends on the choice of ξ. A definition of ξ from a model of the fracture process or the crack-tip deformation [Leichti and Chai, 1992; Kim, 2003] introduces the concept of a cohesive length as an additional fracture parameter. This starts to move the analysis away from a pure LEFM approach, where an energy term is the only required fracture parameter, towards a

---

[1] In practice, some of the details of the geometry and material properties at the crack-tip scale may not be exactly as assumed in the LEFM analysis of an interface crack. For this reason, the term "nominal phase angle", ψ^∞, will be used to describe ψ_K when we don't wish to imply mathematical rigor at the crack-tip scale.

cohesive-zone type of model in which the second fracture parameter in the form of the cohesive strength naturally introduces a length scale into the framework.

In this paper, we shall show how the length scale that evolves from a cohesive-zone model provides a natural link between the nominal phase angle and a mixed-mode failure criterion. Two basic questions provided the initial impetus for the work described in this paper: (i) What is the relationship between the intrinsic cohesive length that controls the phase angle in bi-material systems and the nominal cohesive length that is defined in terms of the cohesive parameters? (ii) How does this relationship depend on the shape of the cohesive law? These questions were addressed by first examining mixed-mode fracture when $\beta = 0$. Under these conditions, there is a regime in which crack propagation can be well defined within an LEFM framework, and any valid mixed-mode cohesive-zone model must reproduce the phase angle predicted from LEFM, with no dependence on the details of the cohesive laws. Once this was demonstrated, the cohesive-zone model was used to explore conditions that deviated from those required for LEFM and also to explore the case of $\beta \neq 0$.

2. Analytical and numerical approaches

2.1 Linear elastic solutions

The beam-like geometries described by Suo and Hutchinson [1990] were used to explore mixed-mode interfacial fracture in this study. As shown in Fig. 2, these consist of two beams of thickness h_1 and h_2 bonded across an interface containing a crack and loaded only by axial loads, N, and moments, M. The more general loading associated with transverse shear [Li *et al.*, 2004] was not considered in this study, as the LEFM solutions have not been extended to include the effects of non-zero values of β. The

complex stress-intensity factors, K_N and K_M, for the two separate problems shown in Fig. 2, one defined only by axial loads and the other defined only by moments, is given by [Suo and Hutchinson, 1990]

$$K_N = \frac{\rho N}{\sqrt{2Uh_1}} e^{i\omega_N} h_1^{-i\varepsilon} \tag{10a}$$

$$K_M = \frac{\rho M}{\sqrt{2Vh_1^3}} e^{i(\omega_N - \phi_{MN})} h_1^{-i\varepsilon} \tag{10b}$$

where the phase shift between K_M and K_N is given by

$$\cos\phi_{MN} = 6\Sigma H^2(1+H)\sqrt{UV} \quad .$$

The other parameters in Eqn. (10) are

$$U = \frac{1}{1+\Sigma\left(4H+6H^2+3H^3\right)} \quad ,$$

$$V = \frac{1}{12\left(1+\Sigma H^3\right)} \quad ,$$

$$\Sigma = \frac{1+\alpha}{1-\alpha}, \qquad H = \frac{h_1}{h_2}, \qquad \rho = \sqrt{\frac{1-\alpha}{1-\beta^2}},$$

and ω_N is a function of α, β and H given in Suo and Hutchinson [1990].[2] The stress-intensity factor for combined loading, K_{MN}, is equal to $K_M + K_N$. The obvious choice of characteristic length in Eqn. 9 is h_1, so the nominal phase angle for this combined loading is

$$\psi^\infty = \tan^{-1}\left[\frac{\mathrm{Im}\left(K_{MN}h_1^{i\varepsilon}\right)}{\mathrm{Re}\left(K_{MN}h_1^{i\varepsilon}\right)}\right] = \tan^{-1}\left[\frac{\eta\sin\omega_N + \sin\left(\omega_N - \phi_{MN}\right)}{\eta\cos\omega_N + \cos\left(\omega_N - \phi_{MN}\right)}\right], \tag{11}$$

where $\eta = \sqrt{V/U}\left(Nh_1/M\right)$. The use of a different characteristic length, ξ, changes the phase angle to

$$\psi_\xi = \psi^\infty + \varepsilon\ln\left(\xi/h_1\right) \tag{12}$$

---

[2] $\omega_M = \omega_N - \phi_{MN}$ is also given in Li *et al.* [2004] for $\beta = 0$ and other values of H. These values were used for some calculations in this paper to avoid uncertainties from interpolation.

2.2 Cohesive-zone model

The 2-D mixed-mode cohesive-zone model used in this paper follows that developed by Yang and Thouless [2001] in which two distinct relationships are used for the opening (mode I) and shear (mode II) traction-separation laws, as indicated schematically in Fig. 3. In this model, the two modes are coupled only through a failure criterion that gives the critical combination of opening and shear displacements at which the tractions in both modes fail simultaneously. This type of mixed-mode law has been shown to have predictive capabilities for some adhesive joints [Yang and Thouless, 2001]. It is recognized that there are physical problems for which deformation in one mode may be expected to affect the details of the constitutive behavior in the other mode. However, for the purposes of the present paper, the model provides a useful simplification in the number of parameters required to describe the cohesive laws, and the general concepts for the behavior of mixed-mode cohesive laws elucidated in this paper should extend to these other types of models. In particular, the robust reduction to LEFM results when the fracture length scale is small that will be demonstrated in this paper, must be reproduced in any valid cohesive-zone model.

In the cohesive-zone model used in this study, the tractions across the interface independently follow the traction-separation curves appropriate to the mode of deformation as the crack surfaces move relative to each other. At any increment of loading, the area swept out under the appropriate traction-separation law at any point ahead of the crack tip is $\mathcal{W}_{\mathrm{I}}$ for the mode-I tractions and $\mathcal{W}_{\mathrm{II}}$ for the mode-II tractions

(Fig. 3).[3] The areas swept out under the two traction-separation curves at the crack tip (the first element for which both tractions are non-zero) can be designated as $\mathcal{W}_{\mathrm{Io}}$ and $\mathcal{W}_{\mathrm{IIo}}$, and if the materials on either side of the interface are elastic, the *J*-integral at the crack tip is [Budiansky, 1986]:

$$J = J_I + J_{II} = \mathcal{W}_{Io} + \mathcal{W}_{IIo} \ , \tag{13}$$

where J_I and J_{II} are the mode-I and mode-II components of the *J*-integral. Following the form of Eqn. (7), it is then possible to write a general definition for the crack-tip phase angle in a cohesive-zone model as

$$\psi_o = \tan^{-1}\sqrt{\mathcal{W}_{IIo}/\mathcal{W}_{Io}} \quad . \tag{14}$$

Parmigiani and Thouless [2007] have verified that, for one particular form of cohesive law, when $\beta = 0$ and the cohesive length is small enough, this crack-tip phase angle, ψ_o, is identical to the nominal phase angle defined by Eqn. 7. It should be emphasized that alternative definitions for the phase angle based on displacements or stress, rather than energy, that are often used in the cohesive-zone literature will generally be dependent on the shape of the cohesive-law, and will not match LEFM values except by serendipity.

A number of authors have proposed that the shape of the traction-separation law may influence the behavior of cohesive-zone models [Chandra *et al.*, 2002; Volokh, 2004; Alfano, 2006]. Therefore, different forms of the cohesive laws were used in this study to explore how different cohesive laws affect the concepts of mixed-mode fracture.

---

[3] As implemented in this study, $\mathcal{W}_{\mathrm{I}}$ and $\mathcal{W}_{\mathrm{II}}$ are not realized as energy losses until failure of the element has occurred - non-linear elastic traction-separation laws are being used. Again, this was done to minimize the number of parameters needed to describe the laws. Only for problems in which the cohesive tractions unload before failure would any difference between elastic and inelastic laws be realized. There are several scenarios in which this could be an issue, including problems for which $\beta \neq 0$, but in the interests of focus and space, this complication is not developed further.

In particular, a tri-linear shape was chosen for both modes of deformation, since this is a general form that can describe a wide range of different behaviors by means of changing only a few non-dimensional parameters. The details of this law are best described by reference to Fig. 4. In mode I, the relationship between normal stress and normal displacement is given by

$$\sigma = \frac{\hat{\sigma}_a}{\delta_{Ia}}\delta_I \qquad \delta_I < \delta_{Ia}$$

$$\sigma = \hat{\sigma}_a - \frac{\hat{\sigma}_a - \hat{\sigma}_b}{\delta_{Ib} - \delta_{Ia}}\left(\delta_I - \delta_{Ia}\right) \qquad \delta_{Ia} \le \delta_I < \delta_{Ib}$$

$$\sigma = \hat{\sigma}_b - \frac{\hat{\sigma}_b}{\delta_{Ic} - \delta_{Ib}}\left(\delta_I - \delta_{Ib}\right) \qquad \delta_{Ib} \le \delta_I < \delta_{Ic} \qquad \text{(15a)}$$

The stiffness for negative mode-I displacements is identical to the initial stiffness for positive displacements. In mode II, the relationship between shear stress and shear displacement is given by

$$\tau = \frac{\hat{\tau}_a}{\delta_{IIa}}\delta_{II} \qquad \delta_{II} < \delta_{IIa}$$

$$\tau = \hat{\tau}_a - \frac{\hat{\tau}_a - \hat{\tau}_b}{\delta_{IIb} - \delta_{IIa}}\left(\delta_{II} - \delta_{IIa}\right) \qquad \delta_{IIa} \le \delta_{II} < \delta_{IIb}$$

$$\tau = \hat{\tau}_b - \frac{\hat{\tau}_b}{\delta_{IIc} - \delta_{IIb}}\left(\delta_{II} - \delta_{IIb}\right) \qquad \delta_{IIb} \le \delta_{II} < \delta_{IIc} \qquad \text{(15b)}$$

The shear stresses for negative shear displacements follow the same relationships, except the sign of the shear stress is reversed. Since a finite thickness was always used for the cohesive elements, compressive stresses (negative mode I) could be accommodated across the interface, without resorting to contact elements. It was always verified that negative mode-I displacements were always less than the thickness of the cohesive elements during the calculations presented in this paper.

In the results that follow, the tri-linear laws are described by three non-dimensional shape parameters for each mode: δ_a/δ_c, δ_b/δ_c and R, where $R_I = \hat{\sigma}_a/\hat{\sigma}_b$ and $R_{II} = \hat{\tau}_a/\hat{\tau}_b$. The total area under each traction-separation curve is designated by the mode-I and mode-II toughness values, Γ_I and Γ_{II}. The two cohesive strengths, $\hat{\sigma}$ and $\hat{\tau}$, that are used in the definition of the cohesive length for each mode (Eqn. 1) are the largest of $\hat{\sigma}_a$ or $\hat{\sigma}_b$ and $\hat{\tau}_a$ or $\hat{\tau}_b$, respectively. By varying the three shape parameters it is possible to describe (i) linear-hardening laws ($\delta_a/\delta_c = \delta_b/\delta_c = R = 1$), (ii) linear-softening laws ($\delta_a/\delta_c = \delta_b/\delta_c = 0$; $R = 1$), (iii) constant stress laws ($\delta_a/\delta_c = 0$; $\delta_b/\delta_c = R = 1$), (iv) saw-tooth laws ($\delta_a/\delta_c = \delta_b/\delta_c$; $R = 1$), and (v) trapezoidal laws ($\delta_a/\delta_c \neq \delta_b/\delta_c$; $R = 1$). It is also possible to describe double-peak laws that provide models for interfaces with two characteristic strengths such as fiber-reinforced composites [Li *et al.*, 2005]: $R > 1$, if the initiation or matrix-cracking strength is greater than the bridging or fiber-bundle strength, and $R < 1$, if the initiation or matrix strength is less than the bridging or fiber-bundle strength.

3. Results

The cohesive-zone model discussed above was used to analyze mixed-mode geometries of the form shown in Fig. 2. Three- and four-node, fully-integrated, two-dimensional, plane-strain, linear-elastic, continuum elements were used, with an unstructured mesh. Cohesive elements with the traction-separation law described in the previous section were placed all the way along the interface, with the thickness of the cohesive zone being set at $t/h_2 = 1/12{,}500$. The cohesive model was implemented in a user-defined element (UEL) definition in ABAQUS v6.7 with a Fortran subroutine as originally developed by Yang *et al*. [1999], and extended for mixed-mode conditions

[Yang and Thouless, 2001]. A specific example of the mesh and loading used is shown in Fig. 5. External loads and moments were applied as distributed surface forces where appropriate. The necessary extent of mesh refinement was determined by trial and error until discrepancies were within an acceptable level of uncertainty that is reflected by the magnitude of error bars on the plots presented in this paper. The required size, l_{max}, for the cohesive-zone elements was about $l_{max}/h_1 \approx 2 - 3 \times 10^{-4}$ for the range of cohesive-length scales considered. This ensured that the ratio of the nominal cohesive-length scale to the cohesive-zone element size, $\overline{E}^{*}\Gamma_I / \hat{\sigma}^2 l_{\max}$, was greater than about 300.

3.1 Effects of cohesive law on phase angle for $\beta = 0$

The concept of a phase angle, given in Eqn. 14 for a cohesive-zone framework, can be expanded so that it is defined as a local phase angle at any element along the interface:

$$\psi = \tan^{-1}\sqrt{w_{II} / w_I} \quad . \tag{16}$$

This local phase angle calculated for a geometry loaded only by an axial couple (as illustrated in Fig. 5) is plotted in Fig. 6 as a function of distance along the interface from the crack tip. In this plot the nominal mode-I and mode-II cohesive-length scales, $\zeta_I / h_1 = \overline{E}\Gamma_I / \hat{\sigma}^2 h_1$ and $\zeta_{II} / h_1 = \overline{E}\Gamma_{II} / \hat{\tau}^2 h_1$, are kept relatively small, so that LEFM conditions are expected to prevail. The phase angles greater than 90º at locations remote from the crack tip indicate the compressive loading across the interface that is required to compensate for the opening mode at the crack tip, since there is no net normal force across the interface in this geometry. This compression across the interface is accommodated by the finite thickness of the cohesive zone. Figure 6 reproduces one of the key results of Parmigiani and Thouless [2007] that, for small nominal cohesive-length

scales, the local phase angle along the interface asymptotes at the crack tip to the nominal value given by LEFM [Suo and Hutchinson, 1990]. The important new result demonstrated in this paper is that this agreement between the asymptotic crack-tip phase angle and the nominal phase angle is a general phenomenon, and does not depend on the choice of cohesive law. Furthermore, although most of the results in the figure have been presented for a subset of cohesive-laws that are identical in both modes, the asymptotic values are robust *provided the nominal cohesive-length scale is small for both mode I and mode II*. This is further illustrated by the set of results (e) shown in Fig. 6, for which the two modes have different shapes of traction-separation laws. The robustness of the crack-tip phase angle is consistent with the expectations that the cohesive law can have no effect on the partition of energy at a crack tip under LEFM conditions. Indeed, reproduction of the LEFM phase angle at small cohesive-length scales is one of the few independent checks that can be made for the validity of cohesive-zone models.[4]

As the nominal cohesive-length scale is increased, LEFM conditions may be violated, and there is no longer any expectation that the crack-tip phase angle should match the nominal phase angle from LEFM. As an example, Fig. 7 shows a gradual shift of the crack-tip phase angle as the nominal cohesive-length scale for each mode is increased. Even though the crack-tip phase angle deviates from the LEFM prediction at larger cohesive-length scales, a plateau in the local phase angle was always observed at the crack tip. The length of this plateau increases with the cohesive length (Fig. 8), but

[4], It should be noted that the shape of a cohesive law may affect predictions of mixed-mode delamination, even under LEFM conditions, through any influence the shape may have on the mixed-mode failure criterion. In this work, we assume that the mode-I and mode-II cohesive laws are coupled through a given mixed-mode failure criterion. Other approaches can result in the mixed-mode failure criterion evolving from coupled cohesive laws. However, in all valid cohesive-zone models the energy partition between the two modes (and, hence, the phase angle) must be consistent with LEFM at small cohesive-length scales.

no relationship between the plateau length and the properties of the cohesive laws has been found.

Figure 9 shows a plot of the normal and shear stresses ahead of the crack tip for the same conditions that were used to calculate the local phase angles shown in Fig. 6. Most of the plots show at least a limited range of distances from the crack tip where the stresses follow the inverse-square-root distribution expected from LEFM. However, this range can be very limited, especially for mode-II. Indeed, for the cohesive law with a constant stress level, there appears to be no portion of the mode-II stress distribution that can be considered to follow the LEFM field. However, it should be noted that this doesn't seem to affect the fact that the crack-tip phase angle asymptotes to the nominal LEFM value. It is also noted that the region in which the stresses might be considered to follow an inverse-square-root distribution is much further away from the crack tip than the length of the plateau over which the local phase angle asymptotes to the nominal value.

3.2 Effects of cohesive law on phase angle for $\beta \neq 0$

Figure 10 shows how the local phase angle varies with distance from the crack tip for several values of β and for a linear-hardening law with nominal cohesive-length scales of $\zeta_I/h_1 = \zeta_{II}/h_1 = 0.1$. As previously illustrated for a different law [Parmigiani and Thouless, 2007], three important features are shown in this figure. First, as with $\beta = 0$, the phase angle asymptotes to a fixed value at the crack tip. Second, this crack-tip phase angle, ψ_o, is different from the nominal phase angle, ψ^∞, that can be calculated from Eqn. 11 [Suo and Hutchinson, 1990]. Third, the difference between ψ_o and ψ^∞

systematically varies with β. These three observations are consistent with Eqn. 12, and this equation can be used to obtain what will be referred to as an intrinsic cohesive length, ξ_o, which controls the shift between the crack-tip phase angle and the nominal phase angle:

$$\psi_0 - \psi^{\infty} = \varepsilon \ln\left(\xi_o / h_1\right) \quad . \tag{17}$$

Therefore, if the nominal phase angle is known for a particular geometry, the shift between the nominal phase angle and the crack-tip phase angle can be used to infer the intrinsic cohesive-length scale, ξ_o/h_1. As shown in Fig. 11, the intrinsic cohesive-length scale is directly proportional to the nominal cohesive-length scale within numerical uncertainty, but the constant of proportionality depends on the nature of the cohesive law.

The shifts in phase angle and the associated cohesive lengths shown in the previous two plots were obtained at one particular instant during loading (the point at which the condition $\mathcal{W}_{Io}/\Gamma_I + \mathcal{W}_{IIo}/\Gamma_{II} = 1$ is met, corresponding to one particular choice of mixed-mode failure criterion). However, the phase angle can be determined at any point during loading, and the possibility that the crack-tip phase angle and cohesive length changes as the applied load is increased has to be considered. Figure 12(a) shows that the phase angle does, indeed, change slightly during loading. However, Fig. 12(b) shows an exception to this generality for linear-hardening laws. The phase angle (and hence the intrinsic cohesive length) remains constant for this type of proportional loading. This is true even when the two modes have different values for the nominal cohesive-length. This observation is probably associated with the fact that linear-hardening laws are unique because the quantities $\overline{E}\mathcal{W}_I/\sigma^2$ and $\overline{E}\mathcal{W}_{II}/\tau^2$ are always constant and equal to ζ_I and ζ_{II}, respectively.

Figure 12(b) also shows that the mode-I and mode-II nominal cohesive lengths have different effects on the crack-tip phase angle. This raises the question of whether there is any effect of nominal phase angle on the intrinsic cohesive-length scale. As shown in Fig. 13, there may be a small effect if the mode-I and mode-II laws have different length scales, but no effect if the two modes have the same length scale. Furthermore, this figure indicates that the intrinsic cohesive-length scale is essentially independent of geometry. The apparent independence of the intrinsic cohesive-length scale from the nominal phase angle and geometry makes the concept of the intrinsic cohesive-length scale appealing. However, the interaction between the mode-I and mode-II length scales complicates the issue in general, especially since all laws other than the linear-hardening ones have intrinsic cohesive-length scales that change during loading.

The results of a concluding set of calculations (Fig. 14) show how the nominal cohesive length might usefully be defined when the modulus mismatch parameter α is not equal to zero.[5] The calculations for this figure were conducted by using identical linear-hardening cohesive laws for modes I and II, and by varying the loading to keep the nominal (and crack-tip) phase angle constant for different values of α. As can be seen

---

[5] A series of numerical studies confirmed that the effective modulus enters the problem only in conjunction with the two values of toughness, as $\overline{E}^* \Gamma_I$ and $\overline{E}^* \Gamma_{II}$. In other words, while the dimensionless group $\overline{E}^* h_1 / \Gamma_I$ enters a dimensional analysis of the problem, it does not appear to affect the results at any cohesive-length scale. This is consistent with LEFM formulations, for which it is well-established that $\overline{E}^*$ appears only as a product with Γ_I and Γ_{II} in an LEFM formulation and that, consequently, there is no length scale associated with the fracture process. However, our numerical results suggest that non-dimensional groups of the form $\overline{E}^* h_1 / \Gamma_I$ are not important, even for large cohesive- lengths where LEFM is violated.

from this figure, the intrinsic cohesive length scaled linearly with a bi-material nominal cohesive length defined using the effective modulus of Eqn. 6:

$$\zeta_I = \overline{E}^* \Gamma_I / \hat{\sigma}^2 \ , \tag{18a}$$

$$\zeta_{II} = \overline{E}^* \Gamma_{II} / \hat{\tau}^2 \quad . \tag{18b}$$

Furthermore, it should be noted that Fig. 14 was developed using various values for β, so it appears that this second modulus mismatch parameter does not enter any definition of the cohesive length.

4. Discussion

The plots of Fig. 9 illustrate the problem with a common approach in the cohesive-zone literature of defining the phase angle either in terms of the ratio of the shear to normal stresses or in terms of the displacements. At the crack tip, where fracture occurs, both of these definitions are completely dependent on the choice of cohesive law. Only for linear-hardening cohesive laws that are identical in both mode-I and mode-II do the definitions based on stress or displacement give a phase angle that is consistent with LEFM. For the particular geometry used in Figs. 6 and 9, a crack-tip "phase angle" based on stress would have varied from 11º to 56º, while a crack tip "phase angle" based on displacement would have varied from 56º to 70º, depending on the choice of cohesive law. These variations in the phase angles should be compared to the constant value of 54-57º (including numerical uncertainty) for all cohesive laws using the definition of phase angle given by Eqn. 14, and to the LEFM value of 55º for this geometry [Li *et al.,* 2004].

By defining the phase angle in terms of the energy partition at the crack tip (Eqn. 14), a connection can be made between analyses for mixed-mode crack growth in

LEFM and in cohesive-zone models. Failure criteria of the form $\Gamma = \Gamma(\psi^{\infty})$ are often used within an LEFM framework. Such criteria can be re-expressed (or approximated) within a cohesive-zone framework in the form of $f\left(\mathcal{W}_{Io}/\Gamma_I,\ \mathcal{W}_{IIo}/\Gamma_{II}\right)=1$ for failure of the crack-tip element (and crack advance). For example, a simple failure criterion that has some of the attributes associated with experimental observations of mixed-mode failure, and that could readily be used within a mixed-mode LEFM analysis is

$$\Gamma = \Gamma\left(\psi^{\infty}\right) = \Gamma_I \frac{\lambda\left(1+\tan^2\psi^{\infty}\right)}{\lambda+\tan^2\psi^{\infty}} \quad , \tag{19}$$

where λ is the ratio between the toughness in mode-I and mode-II: $\lambda = \Gamma_{II}/\Gamma_I$. It can be shown that this is equivalent to a critical condition of

$$\frac{\mathcal{W}_{I_o}}{\Gamma_I} + \frac{\mathcal{W}_{II_o}}{\Gamma_{II}} = 1 \tag{20}$$

when implemented within a cohesive-zone framework. This was used as a condition to define an end point for the mixed-mode calculations of this paper. Other choices for the LEFM mixed-mode failure criteria can be expressed as different criterion for failure of the crack-tip element. None of the significant conclusions of this paper are affected by the choice of failure criterion.

The shape of the cohesive laws can affect mixed-mode fracture in bi-material systems even when the cohesive lengths are small. Furthermore, the intrinsic cohesive length can change during loading for all laws except for the linear-hardening ones. These observations suggest that it might be useful to define an instantaneous cohesive length, perhaps in terms of the average stress experienced by the crack-tip element:

$$\tilde{\xi}_I = \overline{E}^{*}\mathcal{W}_{Io}/\sigma_{ave}^2 = \overline{E}^{*}\delta_{Io}^2/\mathcal{W}_{Io} \quad , \tag{21}$$

where σ_{ave} is the average stress of the traction-separation law for the crack-tip element up

to a displacement δ_{lo}. This concept that the average cohesive strength, rather than the peak cohesive strength, controls fracture is supported by experimental evidence given by Li *et al* [2005]. This work showed that there were two characteristic cohesive-length scales associated with a single traction-separation law that could be used to describe the entire process of matrix cracking and fiber bridging. One small length scale was associated with the high strength and low toughness of matrix cracking; this controlled fracture at small scales, for example, in the absence of a macroscopic crack. A second larger length scale was associated with the relatively low stress and high toughness of fiber bridging; this controlled the propagation of large cracks in fracture specimens. An instantaneous cohesive-length scale (Eqn. 21) naturally provides a smooth transition between the two length scales within a single definition. This concept of an instantaneous cohesive length is being explored further in a companion study.

5. Conclusions

A phase angle that is defined in terms of the partition of energy into shear and normal components, asymptotes to a constant value at the crack tip in a cohesive zone. When the cohesive-length scales are sufficiently small, this asymptotic phase angle is in agreement with the value predicted by LEFM analyses, provided that $\beta = 0$, so the phase angle is well-defined . The stress field in the immediate vicinity of the crack tip (where this phase angle operates) does *not* follow the inverse square root dependence, although there can be a *K*-dominated stress field outside this crack-tip region.

The complications in the definition of a phase angle that are introduced by LEFM when $\beta \neq 0$ can be rationalized by the cohesive-length scales that are inherent to cohesive-zone models of fracture. The intrinsic cohesive-length that dictates the crack-

tip phase angle is proportional to the nominal cohesive length, defined in terms of the toughness and strength. It is also proportional to the effective bi-material modulus. The dependence of the intrinsic cohesive length on the shape of the cohesive-laws for the two modes is not clear. However, the results indicate that the cohesive length may be more usefully defined in terms of an average strength, rather than the peak strength.

The connection between the cohesive parameters, the cohesive-length scale and the crack-tip phase angle that controls fracture appears to be quite robust within the cohesive-zone framework used in this study. Although it is beyond the scope of this present paper, it should be possible to explore these issues for other types of cohesive-zone models, where the modes of deformation might be more tightly coupled. However, it would appear that a key validation for these models should be the correct partition of the energy into the two modes at the crack tip.

6. Acknowledgements

MDT is grateful for the hospitality of Dr. Bent Sørensen at DTU Risø and of Prof. Norman Fleck at Cambridge University during the development of this paper.

References:

Alfano, G. (2006) "On the influence of the shape of the interface law on the application of cohesive-zone models," *Composites Science and Technology*, **66**, 723-730.

Barenblatt, G. I. (1962) "The mathematical theory of equilibrium cracks in brittle fracture," *Advances in Applied Mechanics,* **7**, 55-129.

Bao, G. and Suo, Z. (1992) "Remarks on crack-bridging concepts," *Applied Mechanics Review*, **45**, 355-366.

Budiansky, B. (1986) "Micromechanics II" *Proceedings of the 10th U.S. National Congress of Applied Mechanics*, Austin. TX, 25-32.

Cao, H. C. and Evans, A. G. (1989) "An experimental study of the fracture resistance of bimaterial interfaces," *Mechanics of Materials*, **7,** 295-304.

Chandra, N., Li, H., Shet C., and Ghonem, H. (2002) "Some issues in the application of cohesive zone models for metal-ceramic interfaces," *International Journal of Solids and Structures,* **39**, 2827-2855.

Comninou, M. (1990) "An overview of interface cracks," *Engineering Fracture Mechanics,* **31** (1), 197-208.

Dugdale, D. S. (1960) "Yielding in sheets containing slits," *Journal of the Mechanics and Physics of Solids,* **8**, 100-104.

Dundurs, J. (1969) "Edge-bonded dissimilar orthogonal elastic wedges," *Journal of Applied Mechanics,* **36**, 650-652.

Griffith, A. A. (1920) "The phenomenon of rupture and flow in solids," *Philosophical Transactions of the Royal Society,* **A221**, 163-198.

Hillerborg, A., Modéer, M., and Petersson, P. E. (1976) "Analysis of crack formation and crack growth in concrete by means of fracture mechanics and finite elements," *Cement and Concrete Research*, **6**, 773-782.

Inglis, C. E. (1913) "Stresses in a plate due to the presence of cracks and sharp corners," *Proceedings of the Institute of Naval Architects*, **55**, 219-230.

Jensen, H. M., and Thouless, M. D. (1993) "Effects of residual stresses in the blister test," *International Journal of Solids and Structures*, **30**, 779-795.

Kim, J. H. (2003) "Non-orthogonal stress modes for interfacial fracture based on local plastic dissipation," *Engineering Fracture Mechanics,* **70**, 625-642.

Li, S., Wang, J., and Thouless, M. D. (2004) "The effects of shear on delamination in layered materials," *Journal of Mechanics and Physics of Solids,* **52**, 193-214.

S. Li, M. D. Thouless, A. M. Waas, J. A. Schroeder, and P. D. Zavattieri, "Use of Mode-I Cohesive-Zone Models to Describe the Fracture of an Adhesively-bonded Polymer-Matrix Composite," *Journal of Composites Science & Technology*, **65**, 281-293 (2005).

Liechti, K. M., and Chai, Y. S. (1992) "Asymmetric shielding in interfacial fracture under in-plane shear," *Journal of Applied Mechanics*, **59**, 295-304.

Parmigiani, J. P., and Thouless, M. D. (2007) "The effects of cohesive strength and toughness on mixed-mode delamination of beam-like geometries," *Engineering Fracture Mechanics,* **74**, 2675-2699.

Rice, J. R. (1988) "Elastic fracture mechanics concepts for interfacial cracks," *Journal of Applied Mechanics,* **55**, 98-103.

Rice, J. R., and Sih, G. C. (1965) "Plane problems of cracks in dissimilar media," *Journal of Applied Mechanics*, **32**, 418-423.

Suo, Z., and Hutchinson, J. W. (1990) "Interface crack between two elastic layers," *International Journal of Fracture,* **43**, 1-18.

Thouless, M.D. (1990) "Fracture of a model interface under mixed-mode loading," *Acta Metallurgica et Materialia*, **38**, 1135-1140

Thouless, M. D. (1992). "Mixed-mode fracture of a lubricated interface," *Acta Metallurgica et Materialia*, **40**, 1281-1286.

Tvergaard, V., and Hutchinson, J. W. (1993) "The influence of plasticity on mixed mode interface fracture," *Journal of the Mechanics and Physics of Solids*, **41**, 1119-1135.

Tvergaard, V., and Hutchinson, J. W. (1992). "The relation between crack growth resistance and fracture process parameters in elastic-plastic solids," *Journal of the Mechanics and Physics of Solids, **40***, 1377-1397.

Volokh, K. Y. (2004) "Comparison between cohesive-zone models," *Communication in Numerical Methods in Engineering, **20**, 845-856*

Wang, J. S. and Suo Z. (1990) "Experimental determination of interfacial toughness using brazil-nut sandwich," *Acta metallurgica et materialia*, **38**, 1279-1290.

Q. D. Yang, M. D. Thouless and S. M. Ward, "Numerical Simulations of Adhesively-Bonded Beams Failing with Extensive Plastic Deformation," *J. Mech. Phys. Solids*, **47**, 1337-1353 (1999).

Q. D. Yang and M. D. Thouless, "Mixed-mode fracture analyses of plastically-deforming adhesive joints," *Int. J. Fract.*, **110**, 175-187 (2001).

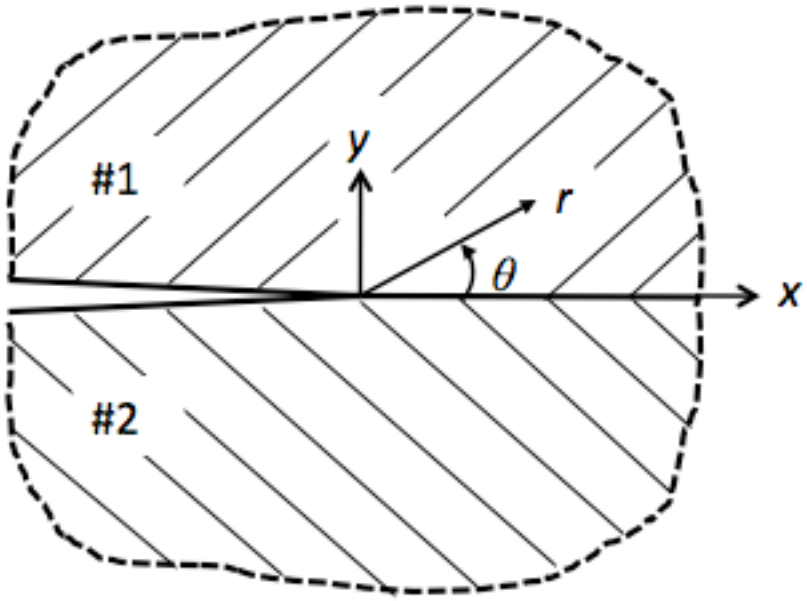

Figure 1: A semi-infinite crack along a bi-material interface with associated coordinate systems.

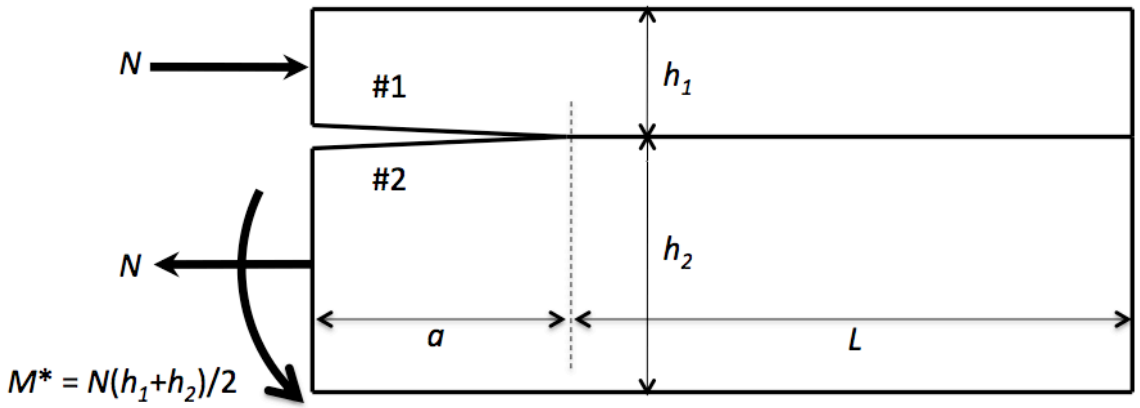

a)

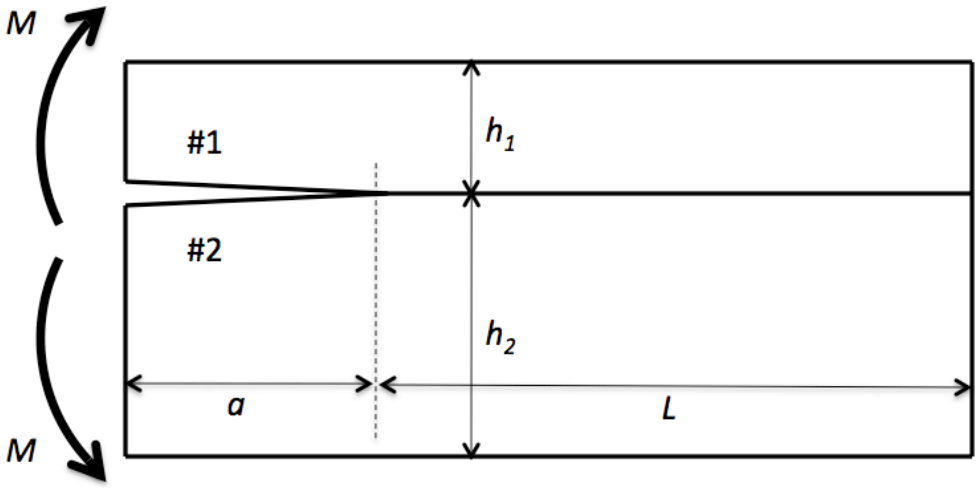

b)

Figure 2: All the geometries analyzed in this paper consist of the superposition of two basic laminated configurations loaded by either **(a)** axial loads, *N*, or **(b)** moments, *M*.

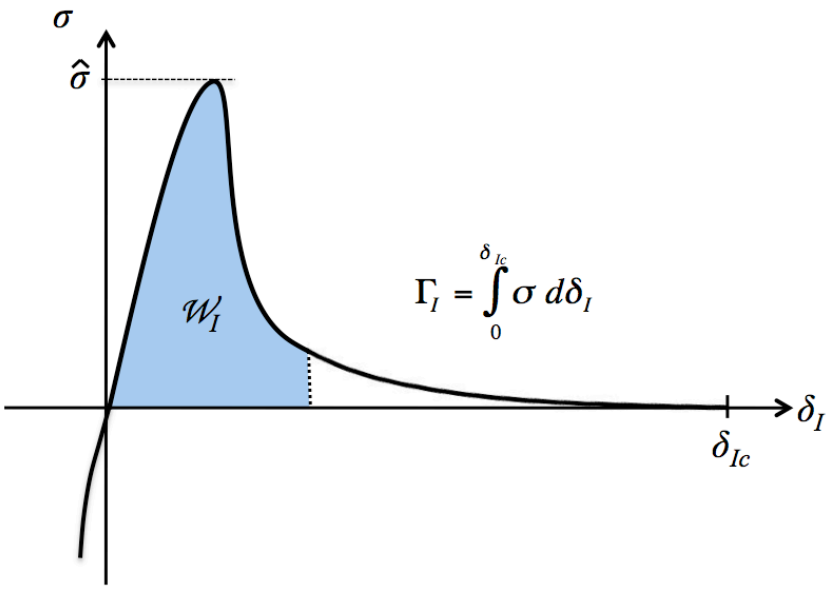

a)

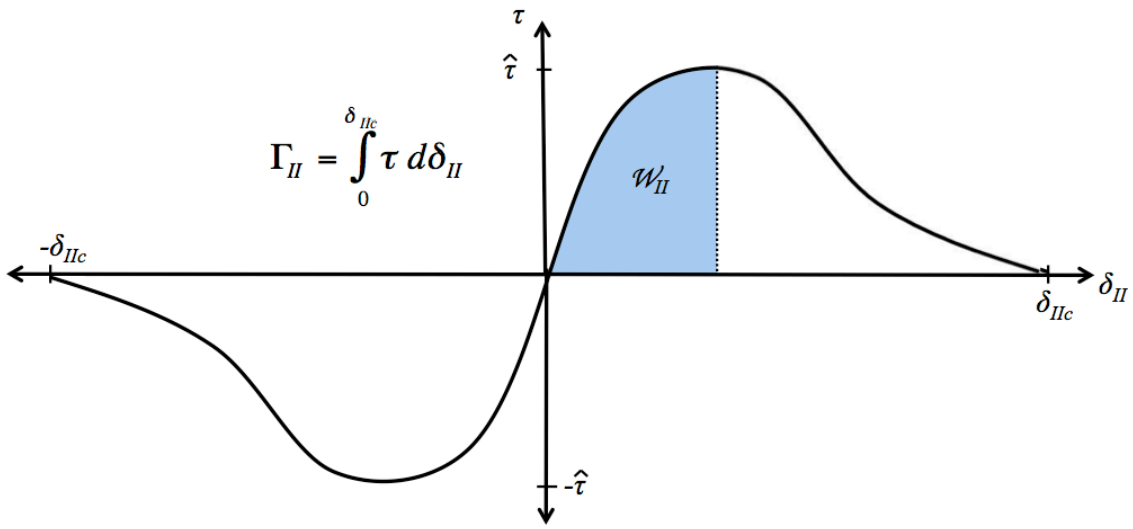

b)

Figure 3: Schematic illustration of **(a)** mode-I and **(b)** mode-II traction-separation laws. Zero displacement corresponds to the equilibrium separation of the interface in these laws.

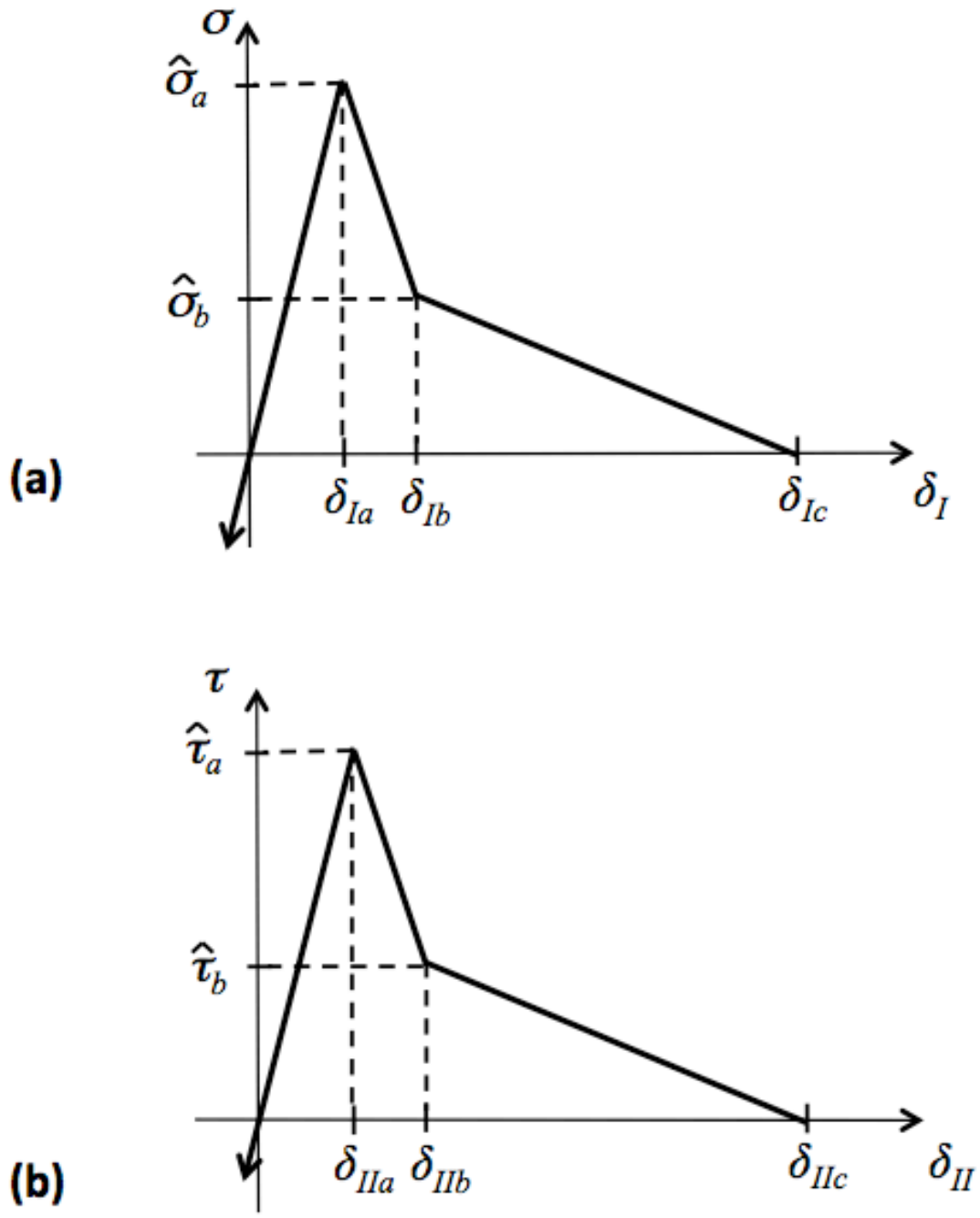

Figure 4: General forms of the **(a)** mode-I and **(b)** mode-II traction-separation laws used in this study. The negative mode-II law is identical to the positive mode-II law. In compression, the stiffness of the mode-I law is the same as the initial stiffness in tension. During the numerical studies, it was always verified that any negative mode-I displacements were less than the thickness of the cohesive elements.

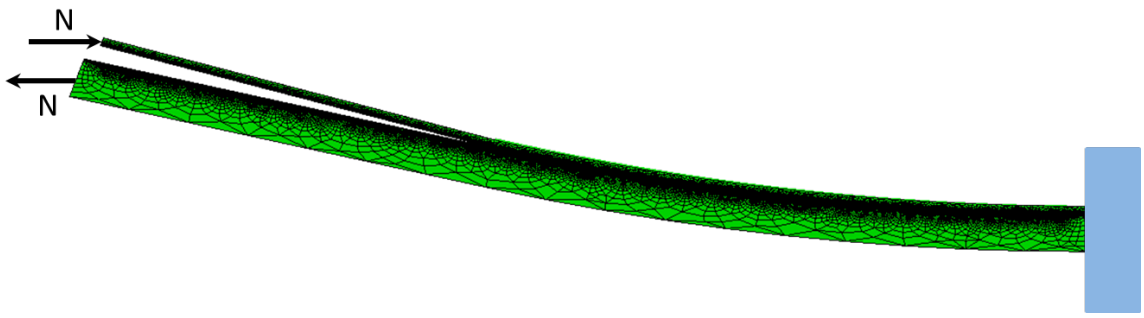

Figure 5: An example of a geometry, mesh and loading used to analyze the mixed-mode problem. In this case an axial couple is applied at the fractured end and a corresponding moment at the unfractured end. Note that the vertical scale is exaggerated, and non-linear deformations were not used in the analyses.

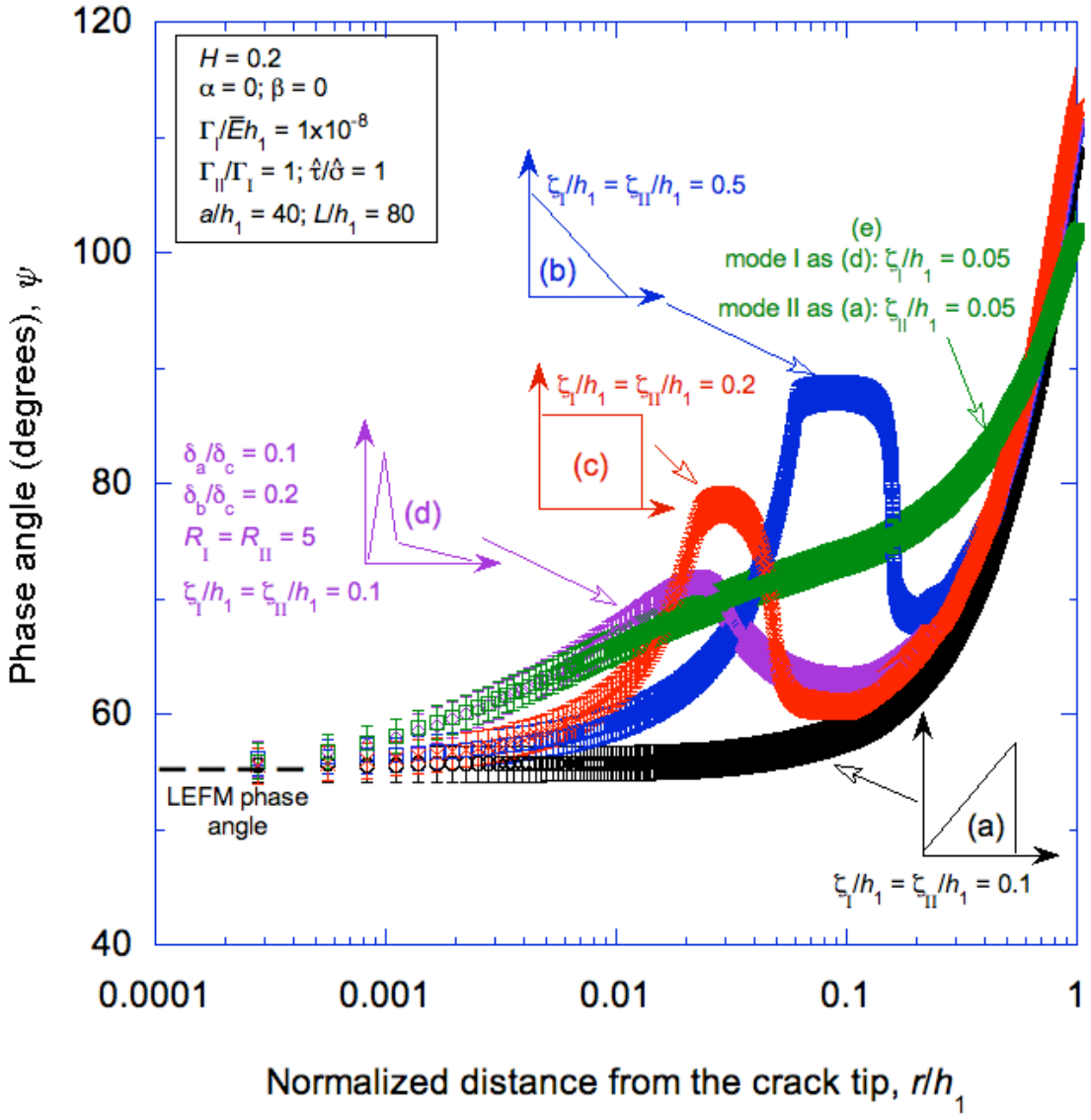

Figure 6: Local phase angle as a function of distance from the crack tip for different cohesive laws. The geometry of the specimen is $H = 0.2$, $a/h_1 = 40$ and $L/h_1 = 80$, with a nominal phase angle of 55.2° [Li *et al*. 2004]. All the laws, except for (e) are identical in modes I and II, and all the laws have $\Gamma_I = \Gamma_{II}$ and $\hat{\sigma} = \hat{\tau}$: (a) is a linear hardening law, with $\zeta_I = \zeta_{II} = 0.1$; (b) is a linear softening law with $\delta_a/\delta_c = 0.001$ and $\delta_b/\delta_c = 0.01$, and $\zeta_I = \zeta_{II} = 0.5$; (c) is a constant-stress law with $\delta_a/\delta_c = 0.01$ and $\delta_b/\delta_c = 0.99$, and $\zeta_I = \zeta_{II} = 0.2$; (d) is a double-peak law with $R = 5$, $\delta_a/\delta_c = 0.1$, $\delta_b/\delta_c = 0.2$, and $\zeta_I = \zeta_{II} = 0.1$; (e) has a double-peak mode-I law with $R = 5$, $\delta_a/\delta_c = 0.1$, $\delta_b/\delta_c = 0.2$, and $\zeta_I = 0.05$, and a linear-hardening mode-II law with $\zeta_{II} = 0.05$. (The data in these plots are taken at the condition where $\mathcal{W}_{Io}/\Gamma_I + \mathcal{W}_{IIo}/\Gamma_{II} = 1$.)

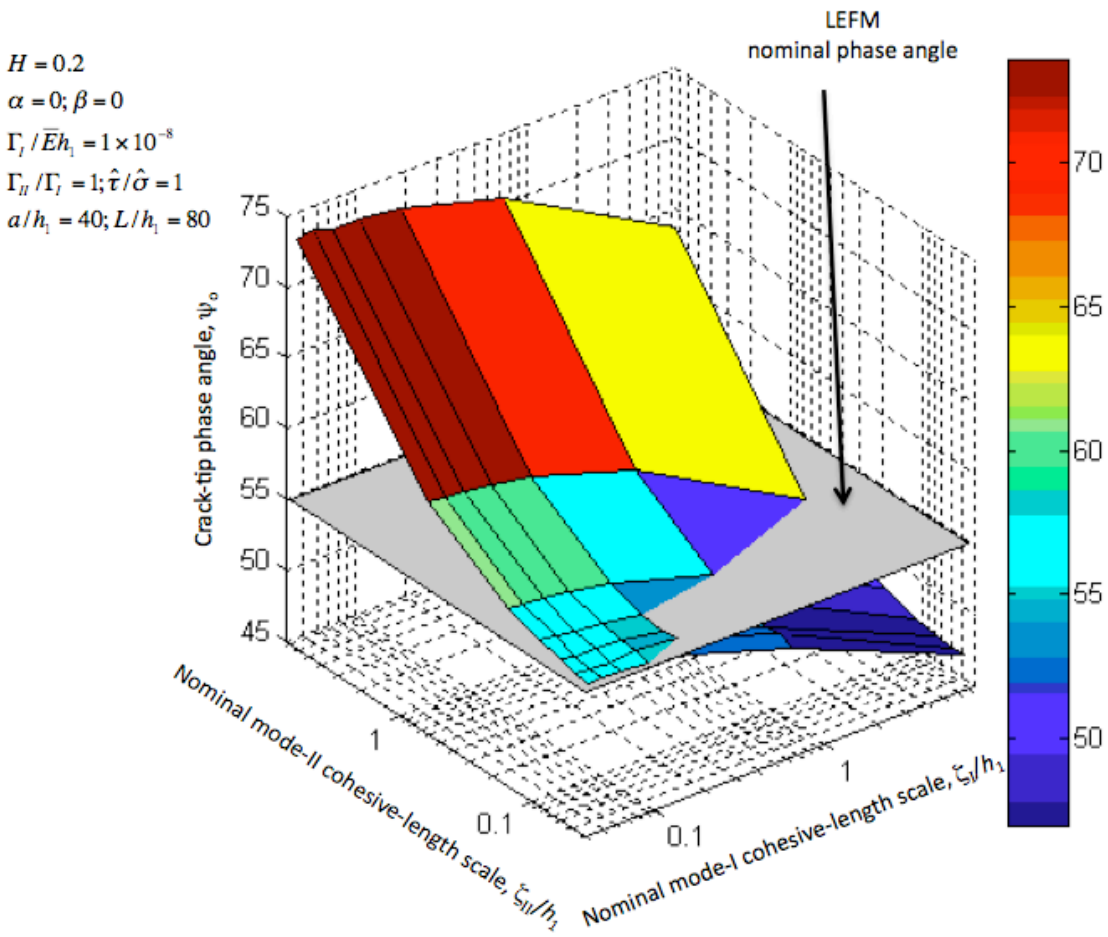

Figure 7: 3-D Plot showing the deviation of the crack-tip phase angle from the nominal value, as the cohesive-length scales in the two modes increase. This plot was obtained using linear-hardening laws for both mode-I and mode-II, with $\Gamma_{II}/\Gamma_I = \hat{\tau}/\hat{\sigma} = 1$, and $\Gamma_I / \bar{E}^* h_1 = 1 \times 10^{-8}$. The geometry of the specimen is H = 0.2, a/h_1 = 40 and L/h_1 = 80, and $\alpha = \beta = 0$ so that the nominal phase angle is 55.2° [Li *et al*. 2004]. (The data in this plot are taken at the condition where $\mathcal{W}_{Io}/\Gamma_I + \mathcal{W}_{IIo}/\Gamma_{II} = 1$.)

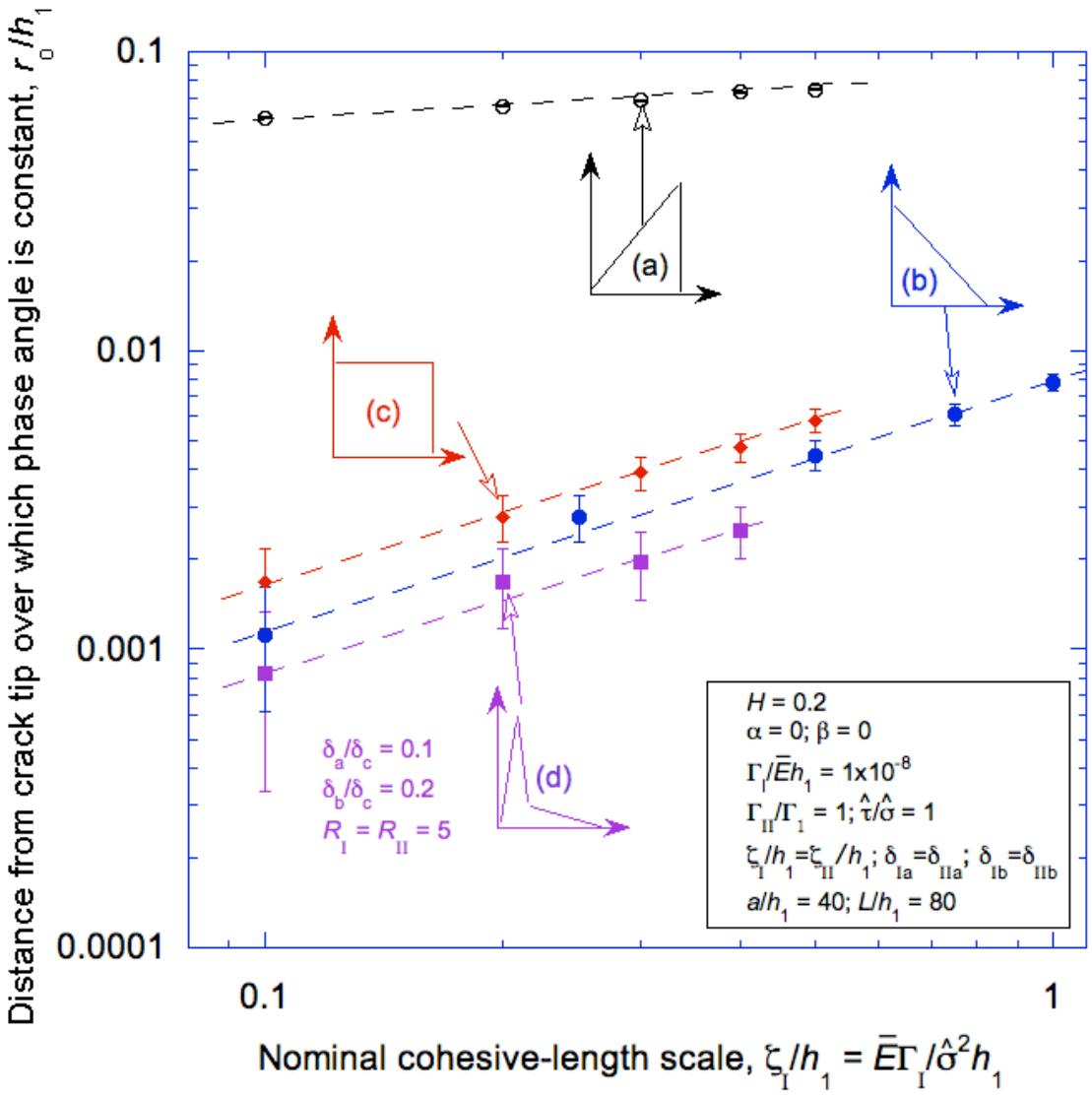

Figure 8: Plot of how the plateau length, r_o, over which the phase angle varies by less than 1.5° depends on nominal cohesive-length scale for different cohesive laws. The mode-I and mode-II traction-separation curves are identical for all the laws: (a) represents a linear hardening law; (b) represents a linear softening law with $\delta_a/\delta_c = 0.001$ and $\delta_b/\delta_c = 0.01$; (c) represents a constant-stress law with $\delta_a/\delta_c = 0.01$ and $\delta_b/\delta_c = 0.99$; (d) represents a double-peak law with $R = 5$, $\delta_a/\delta_c = 0.1$ and $\delta_b/\delta_c = 0.2$. (The data in this plot are taken at the condition where $\mathcal{W}_{Io}/\Gamma_I + \mathcal{W}_{IIo}/\Gamma_{II} = 1$.)

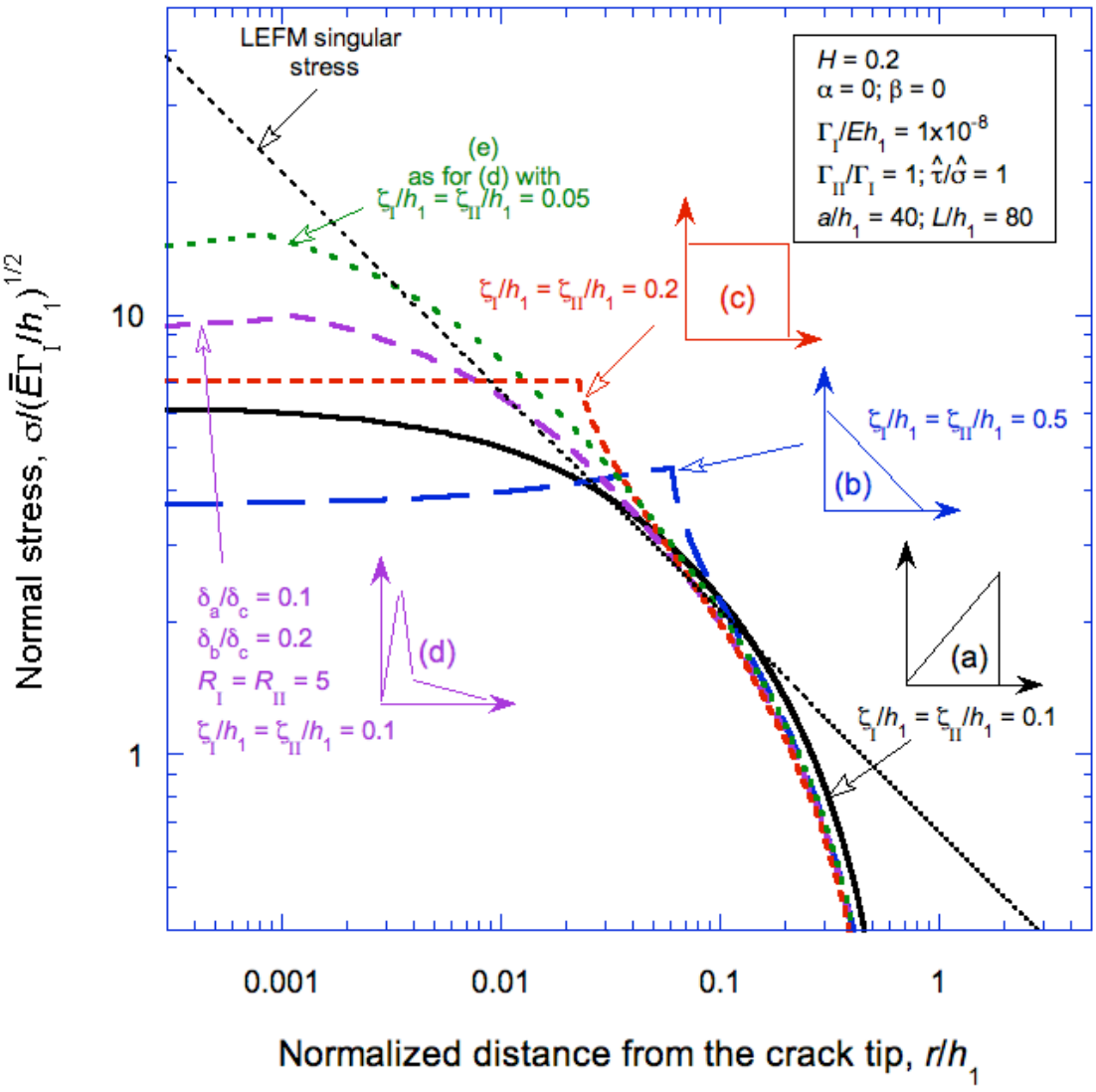
LEFM singular stress
(e)
as for (d) with
$\zeta_I/h_1 = \zeta_{II}/h_1 = 0.05$
$H = 0.2$
$\alpha = 0; \beta = 0$
$\Gamma_I/Eh_1 = 1\text{x}10^{-8}$
$\Gamma_{II}/\Gamma_I = 1; \hat{\tau}/\hat{\sigma} = 1$
$a/h_1 = 40; L/h_1 = 80$
$\zeta_I/h_1 = \zeta_{II}/h_1 = 0.2$
(c)
$\zeta_I/h_1 = \zeta_{II}/h_1 = 0.5$
(b)
(a)
$\zeta_I/h_1 = \zeta_{II}/h_1 = 0.1$
(d)
$\delta_a/\delta_c = 0.1$
$\delta_b/\delta_c = 0.2$
$R_I = R_{II} = 5$
$\zeta_I/h_1 = \zeta_{II}/h_1 = 0.1$
Normal stress, $\sigma/(\bar{E}\Gamma_I/h_1)^{1/2}$
10
1
0.001
0.01
0.1
1
Normalized distance from the crack tip, r/h_1

a)

Figure 9a

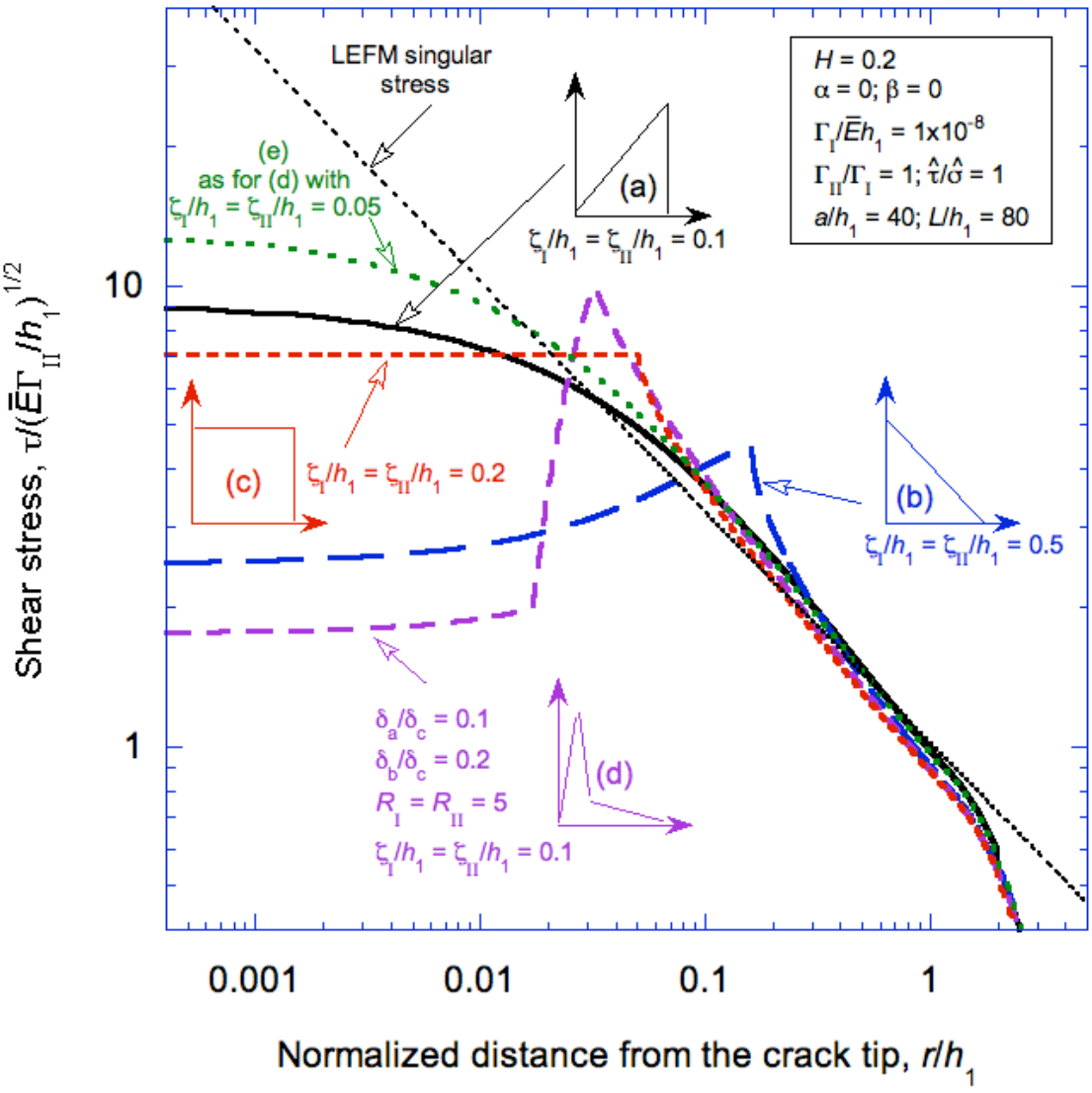

b)

Figure 9: **(a)** Mode-I and **(b)** mode-II stress fields along the interface ahead of an interface crack, with $H = 0.2$, loaded by an axial couple at the fractured end. (The data in this plot are taken at the condition where $\mathcal{W}_{Io}/\Gamma_I + \mathcal{W}_{IIo}/\Gamma_{II} = 1$, so there are finite tractions in both modes I and II in the crack-tip element.)

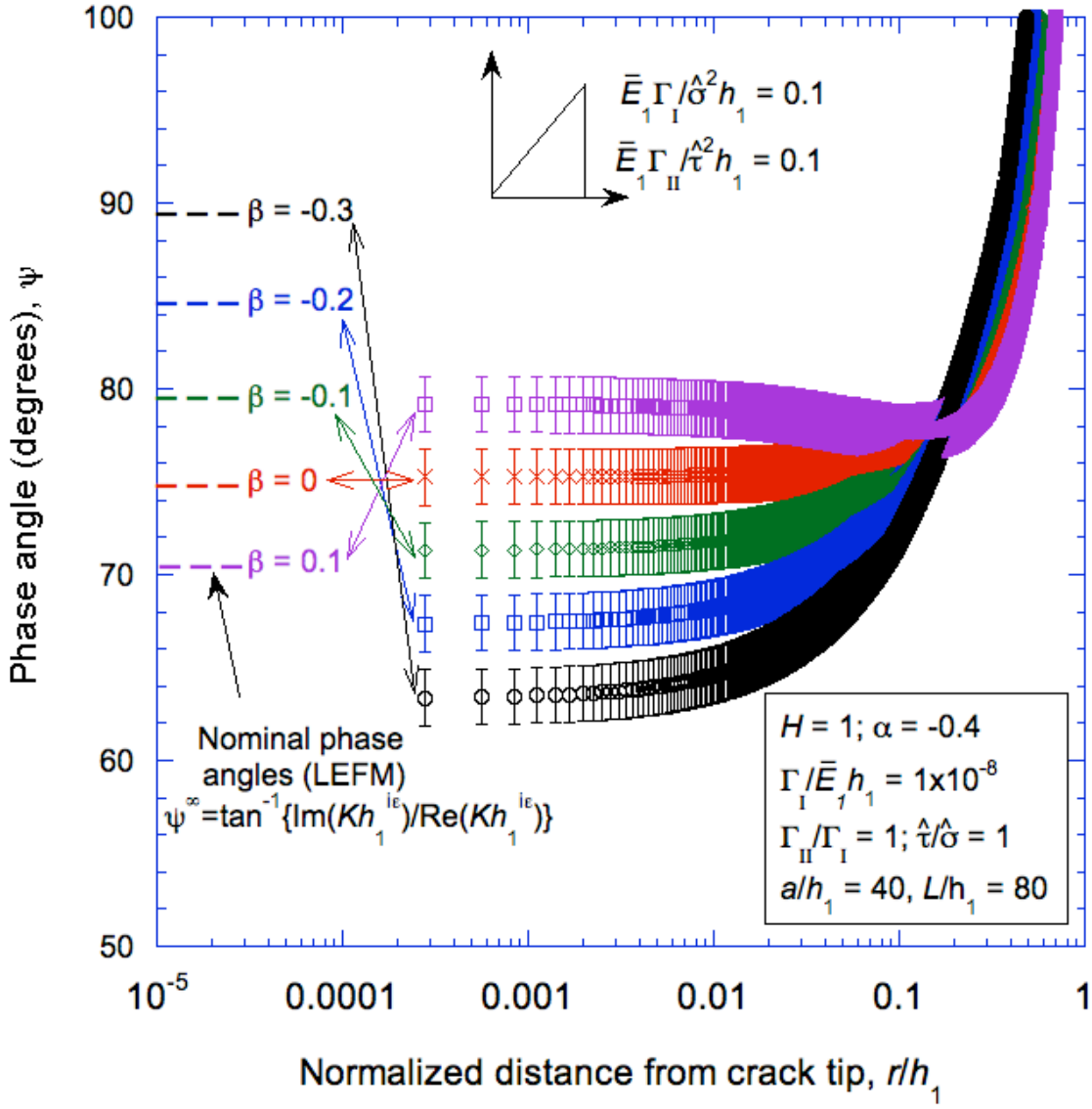

Figure 10: Plot of the phase angle at the point of crack propagation at different positions along the interface for different values of β. (The data in this plot are taken at the condition where $\mathcal{W}_{Io}/\Gamma_I + \mathcal{W}_{IIo}/\Gamma_{II} = 1$.)

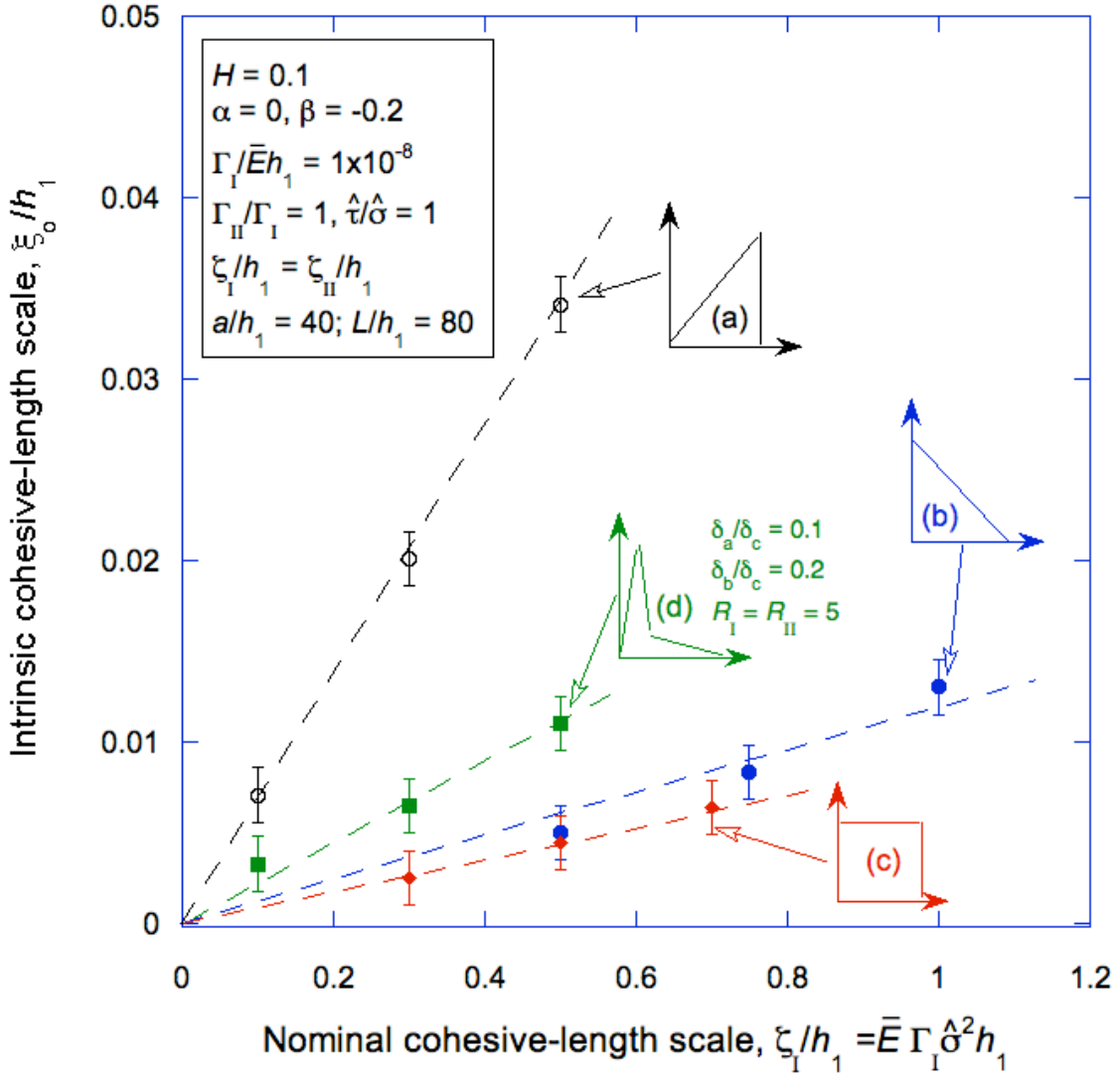

Figure 11: Intrinsic length scale as a function of the nominal cohesive-length scale for various law shapes. (The data in this plot are taken at the condition where $\mathcal{W}_{Io}/\Gamma_I + \mathcal{W}_{IIo}/\Gamma_{II} = 1$.)

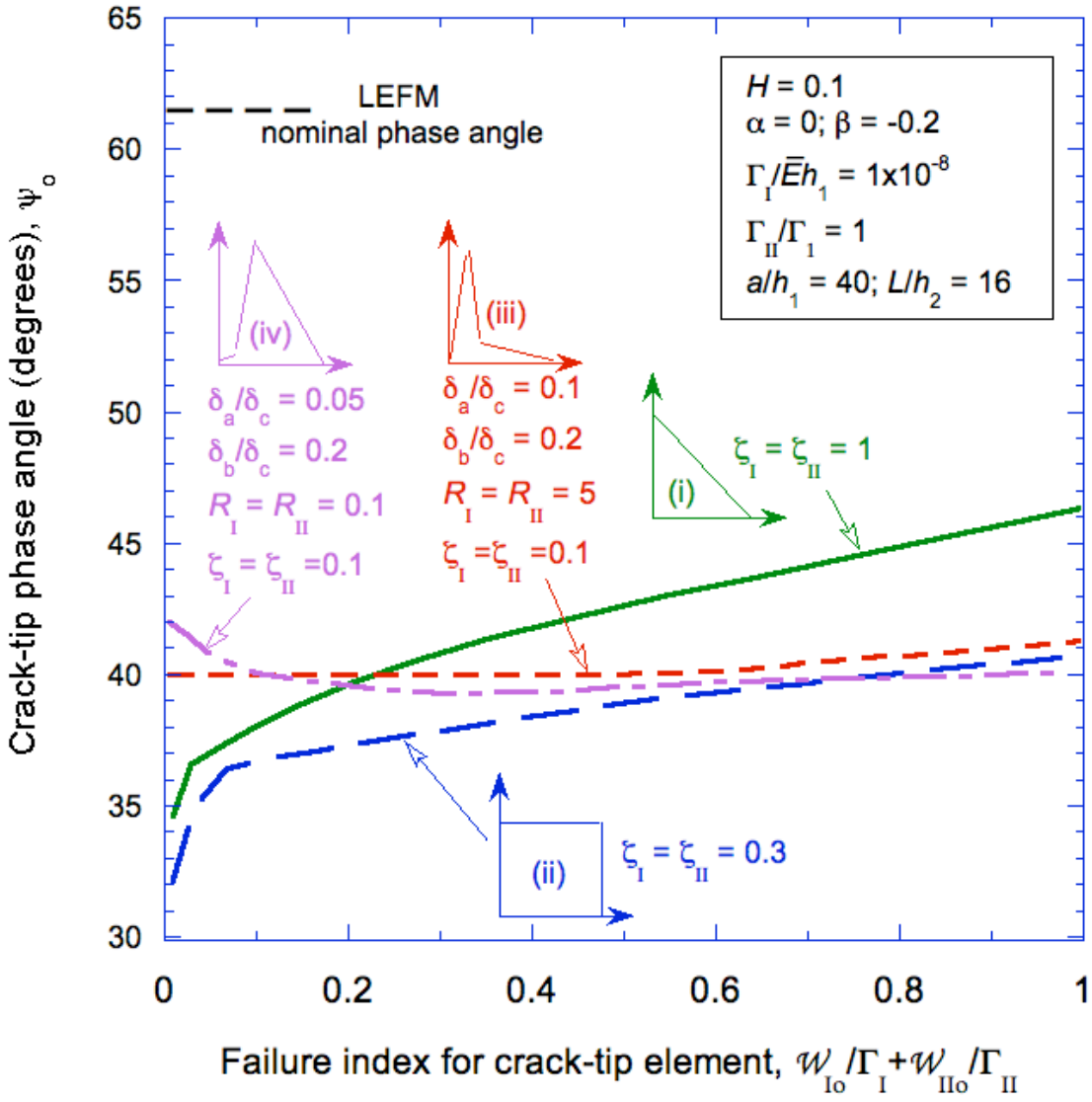
LEFM
nominal phase angle
H = 0.1
α = 0; β = -0.2
Γ_I/Ēh_1 = 1x10^-8
Γ_II/Γ_1 = 1
a/h_1 = 40; L/h_2 = 16
(iv)
δ_a/δ_c = 0.05
δ_b/δ_c = 0.2
R_I = R_II = 0.1
ζ_I = ζ_II =0.1
(iii)
δ_a/δ_c = 0.1
δ_b/δ_c = 0.2
R_I = R_II = 5
ζ_I =ζ_II =0.1
(i)
ζ_I = ζ_II = 1
(ii)
ζ_I = ζ_II = 0.3
Crack-tip phase angle (degrees), ψ_o
Failure index for crack-tip element, w_Io /Γ_I +w_IIo /Γ_II
65
60
55
50
45
40
35
30
0
0.2
0.4
0.6
0.8
1

(a)

Figure 12 (a)

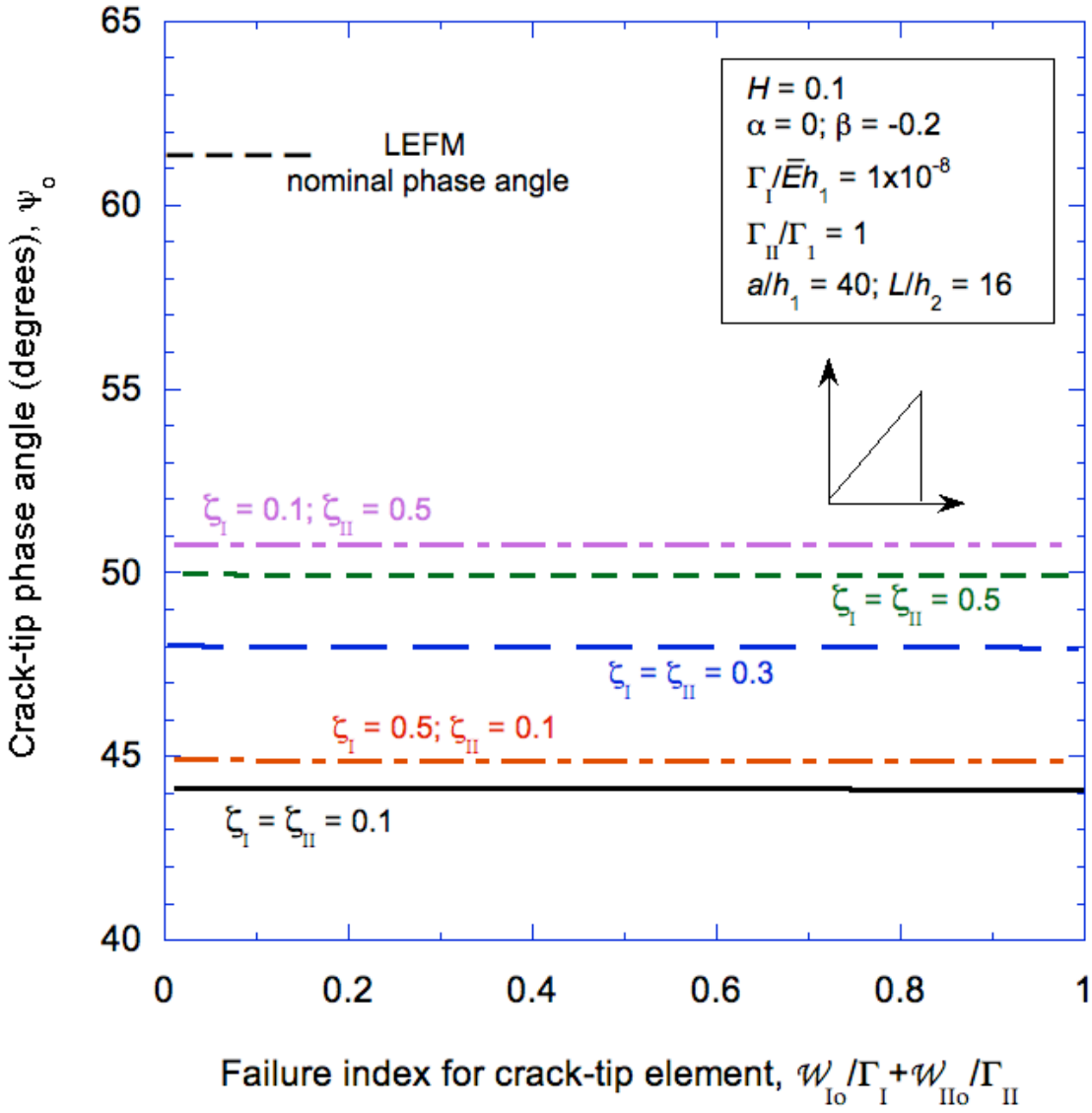

Figure 12 Phase angle as a function of load state for **(a)** different types of cohesive laws and for **(b)** linear-hardening traction-separation laws. The intrinsic cohesive-length scale that controls the crack-tip phase angle changes with loading for all laws except the linear-hardening ones.

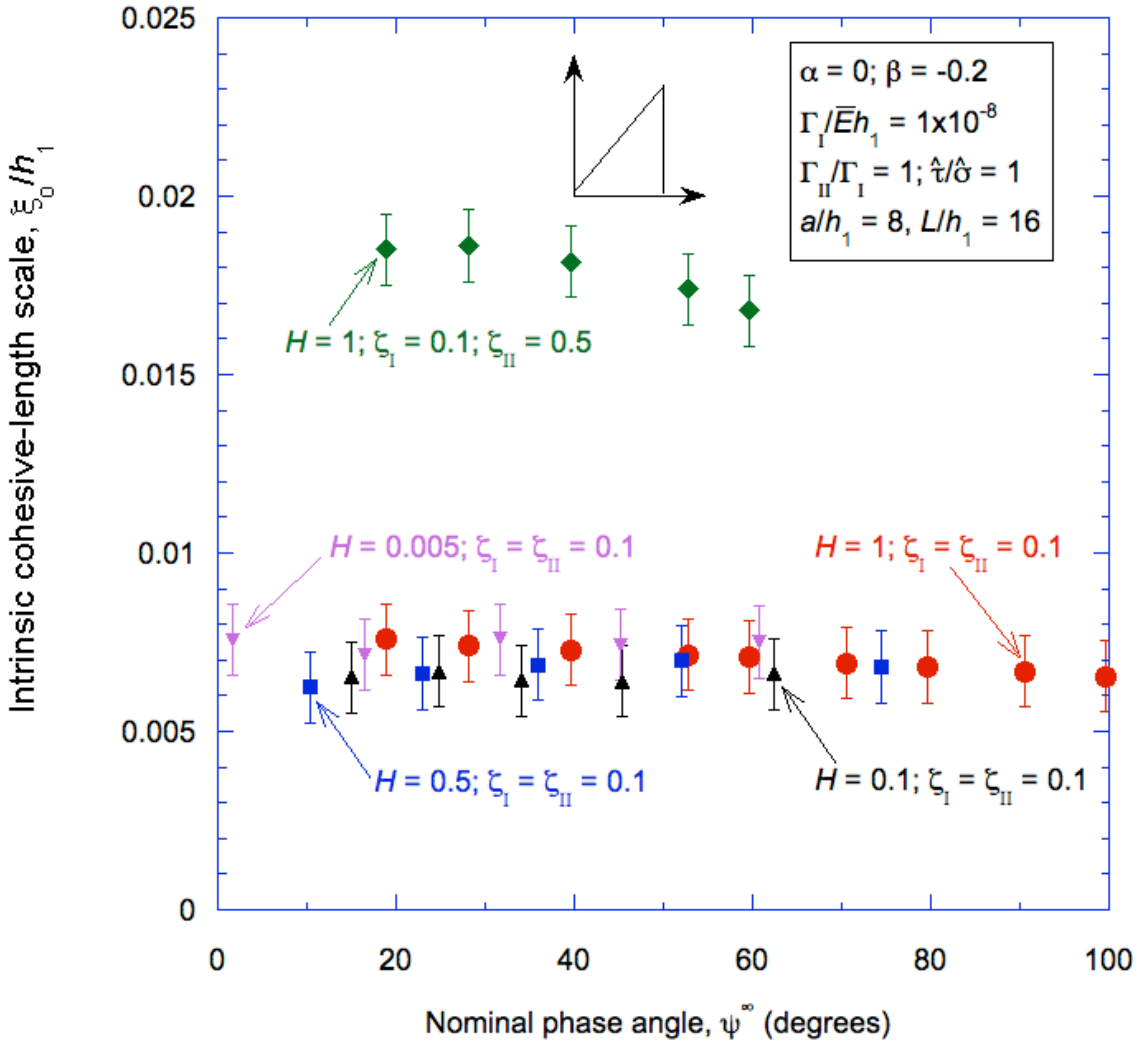

Figure 13: Intrinsic cohesive-length scale plotted as a function of nominal phase angle for a range of beam-like geometries loaded by a moment and axial couples. Linear-hardening laws have been used for the cohesive-zone model, with several different nominal cohesive-length scales in mode-I and mode-II.

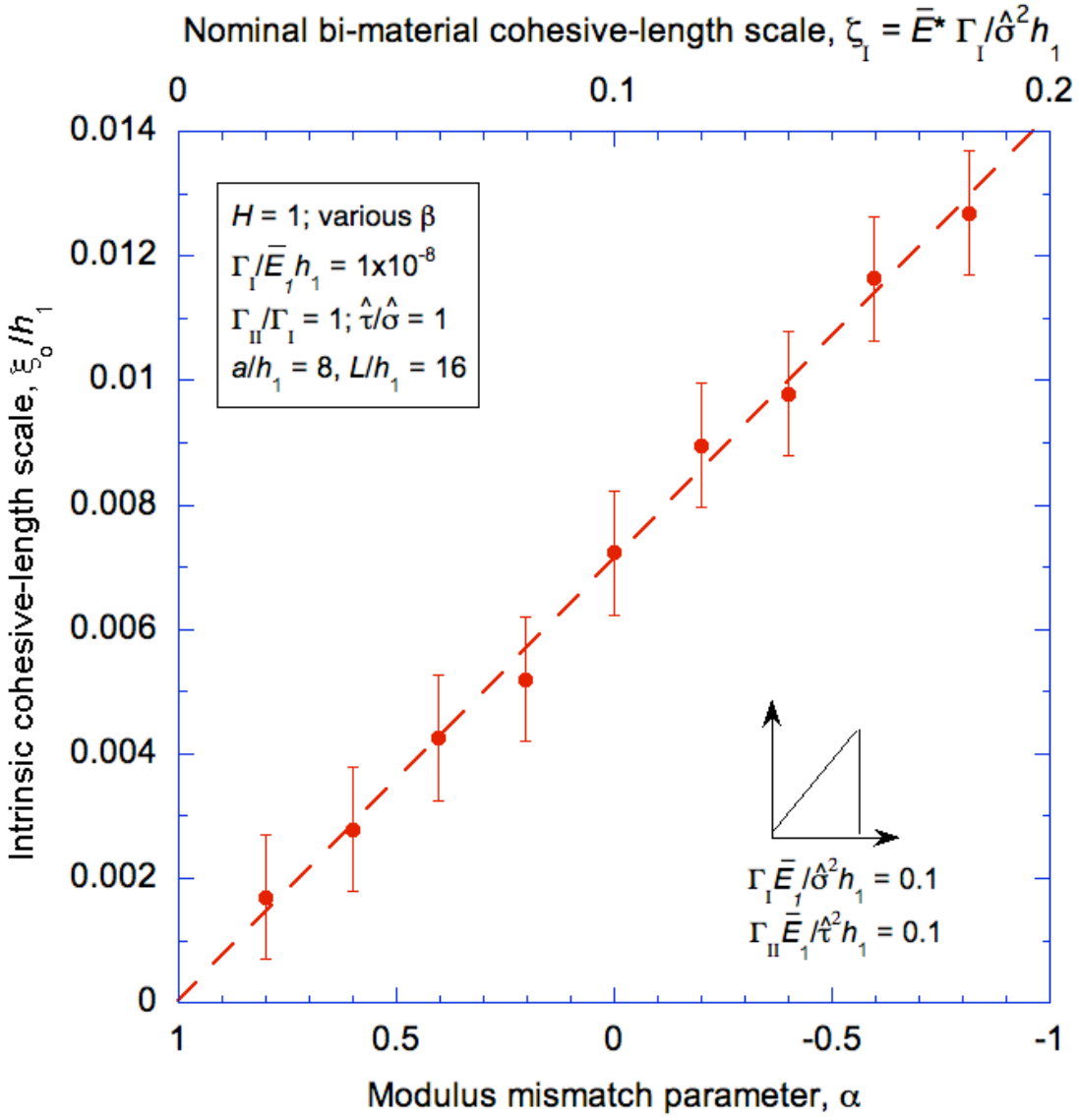

Figure 14: Variation of the cohesive-length scale and intrinsic-length scale with the modulus mismatch, α. The cohesive laws were kept the same for all the data points, so that the only change in the cohesive-length scale came from changes in the modulus. This plot demonstrates that the effective, bi-material modulus, $\bar{E}^*$, is the correct modulus to use in defining the cohesive-length scale of a bi-material system.